Supplementary Information

Double coordination shell modulation of nitrogen-free atomic manganese sites for enhancing oxygen reduction performance

Xue Bai,[a] Yin Wang,[c] Jingyi Han,[a] Siyu Chen,[a] Xiaodi Niu[b,*] and Jingqi Guan[a,*]

[a] Institute of Physical Chemistry, College of Chemistry, Jilin University, 2519 Jiefang Road, Changchun 130021, P. R. China. *E–mail: guanjq@jlu.edu.cn (J.Q. Guan)

[b] College of Food Science and Engineering, Jilin University, Changchun 130062, P. R. China. *E–mail: niuxd@jlu.edu.cn (X.D. Niu)

[c] Inner Mongolia Key Laboratory of Carbon Nanomaterials, Nano Innovation Institute (NII), College of Chemistry and Materials Science, Inner Mongolia Minzu University, Tongliao 028000, China

1. Materials Synthesis

Graphene oxide (GO) was synthesized according to the method described in the literature.[1] 100 mg of GO and 28 mg of $MnSO_4·4H_2O$ were dispersed into 50 mL of deionized water, and a uniformly dispersed suspension was obtained by ultrasound for 45 min. After freeze drying the suspension, a brown solid $MnSO_4$-GO was obtained. The target catalyst Mn-S_1O_4G-600 was obtained by annealing the mixture of $MnSO_4$-GO and sulfur powder in a tube furnace at 600 ℃ in a nitrogen atmosphere for 2 h, and the heating rate was 10 ℃/min. By changing the calcination temperature and doping amount, a series of catalysts were synthesized, namely X%-Mn-S_1O_4G-T, where X = 0.3, 0.5, 0.7, and 0.9, and T = 400, 500, 600, and 700 ℃.

The synthesis of control sample Mn-OG-600 was as follows: $MnCl_2$-GO was directly calcined in a tubular furnace at 600 ℃ for 2 h. Without the addition of $MnSO_4·4H_2O$ precursor, the mixture of GO and sulfur powder was calcined in a tube furnace to obtain SG-600. Without adding both $MnSO_4·4H_2O$ and sulfur powder, OG-600 was obtained under the same conditions.

2. Electrocatalytic characterization

The oxygen reduction performance was tested with a rotating ring-disc electrode (RRDE) and CHI 760E electrochemical workstation, in which the counter electrode is platinum wire, the reference electrode is calomel electrode, and the electrolyte is 0.1 M KOH. Uniform catalyst ink was obtained by dispersing 4 mg catalyst in 400 μL 0.25% nafion/ethanol solution with 30 min of ultrasound. The electrochemical test

was carried out by adding 6 μL of catalyst ink to a RRDE with a diameter of 4 mm. Linear sweep voltammetry (LSV) curve was performed at a sweep speed of 5 mV s^{-1} at rotation rate of 1600 rpm. The cyclic voltammetry (V) curve was performed during the kinetic region (0.6 V-1 V) at a sweep speed of 50 mV s^{-1}. The i-t stability test was performed at 0.6 V.

According to the LSV curves collected at different rotation rates (900, 1225, 1600, 2025, and 2500 rpm), the electron transfer number (n) was calculated from the slope of the K-L equation by their Koutecky-Levich (K-L) diagram (J^{-1} vs. $w^{-1/2}$) linear fit line:[2]

$$\frac{1}{j}=\frac{1}{J_k}+\frac{1}{J_L}=\frac{1}{J_k}+\frac{1}{0.62nFAC_0D_0^{\frac{2}{3}}v^{-\frac{1}{6}}w^{\frac{1}{2}}}$$

The hydrogen peroxide yield (H_2O_2) and electron transfer numbers (n) were obtained from the RRDE using the following equations:

$$n = 4\frac{I_D}{I_D + (I_R / N)}$$

$$H_2O_2 = 200\frac{I_R / N}{I_D + (I_R / N)}$$

The oxygen evolution performance was tested under the same conditions with 0.1 M KOH as electrolyte. Linear sweep voltammetry (LSV) curve was performed at a sweep speed of 5 mV s^{-1}.

3. Zinc–air battery testing

Zn-air battery performances were assessed in 6 M KOH + 0.2 M $Zn(Ac)_2$ on a battery test system (LANHE CT2001A). The anode comprised of a polished zinc plate (0.5 mm in thickness), whereas the cathode was crafted by applying the catalyst ink onto a 1 cm^2 composite carbon substrates surface, achieving a loading of 1 mg cm^{-2}. Catalyst ink was prepared by mixing 100 μL of 1 % Nafion/ethanol solution, 500 μL of ethanol and 2 mg catalyst. The polarization curve was measured at a scan rate of 10 mV s^{-1}. The galvanostatic recharge/discharge cycling measurements were collected at a current density of 5 mA cm^{-2} with each charge and discharge cycle lasting 20 minutes.

4. Computational methods

We employed the Vienna Ab initio Simulation Package (VASP) to investigate the catalytic reaction mechanism of Mn-S_xO_yG models using DFT. The Perdew-Burke-Ernzerhof (PBE) functional was utilized to describe the electronic exchange-correlation interactions during the calculation. A cutoff energy of 300 eV was applied for the plane-wave basis set. To sample the Brillouin zone, we employed a Monkhorst-Pack k-points grid with a 2 × 2 × 1 mesh. Additionally, a sufficiently large vacuum space of 15 Å was included along the z-axis in the supercell configuration. By employing DFT, we computed the Gibbs free energies and determined the 3D structures of *OOH, *O, and *OH species on the surface of the Mn-S_xO_yG models.

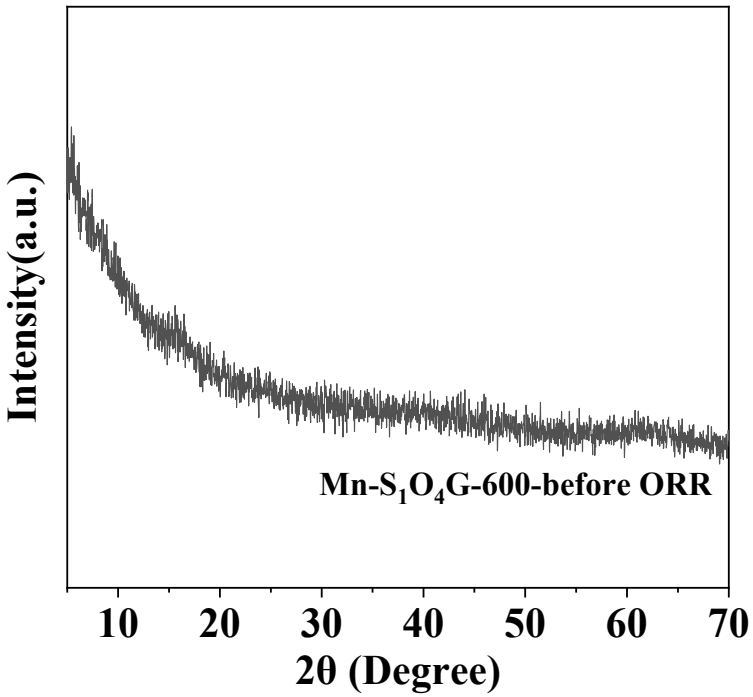

Fig. S1 XRD pattern of Mn-S_1O_4G-600.

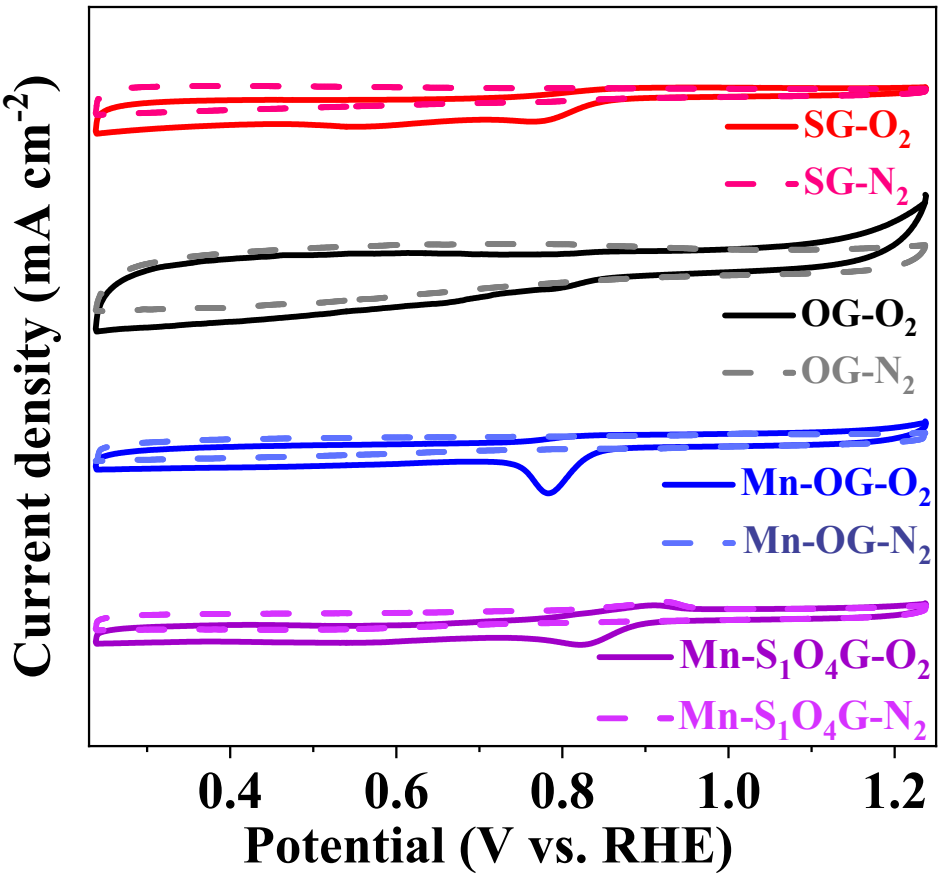

Fig. S2 CV curves of SG-600, OG-600, Mn-OG-600 and Mn-S_1O_4G-600 in N_2- and O_2-saturated 0.1 M KOH (dashed lines: N_2; solid lines: O_2)

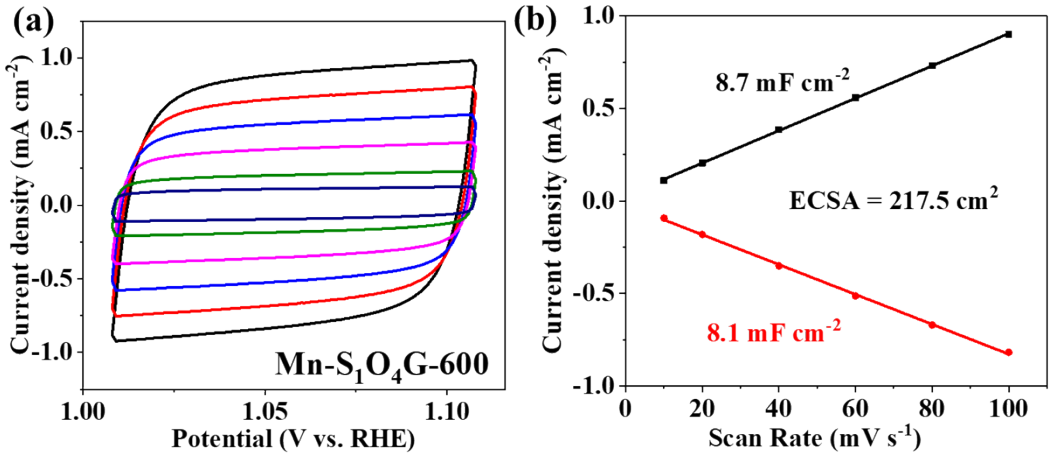

Fig. S3 Cyclic voltammogram curves of the Mn-S_1O_4G-600 at different scan rates for the ORR.

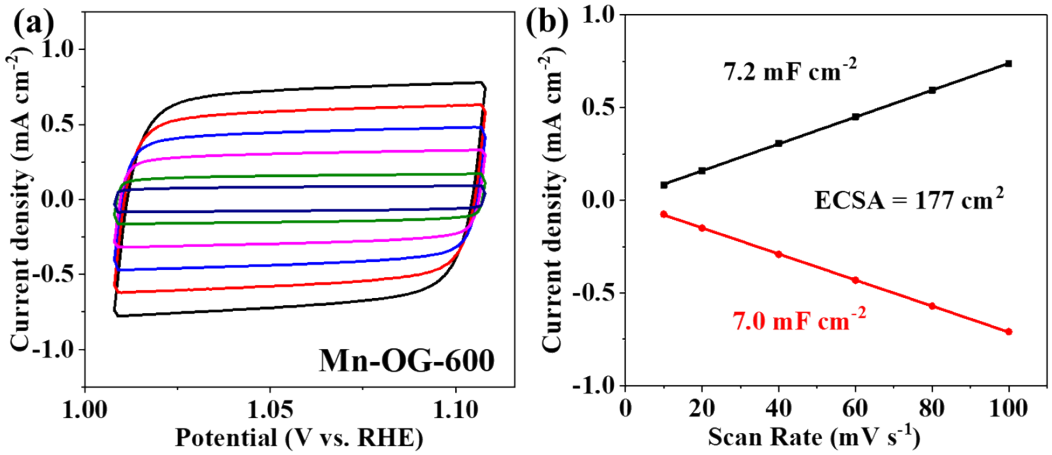

Fig. S4 Cyclic voltammogram curves of the Mn-OG-600 at different scan rates for the ORR.

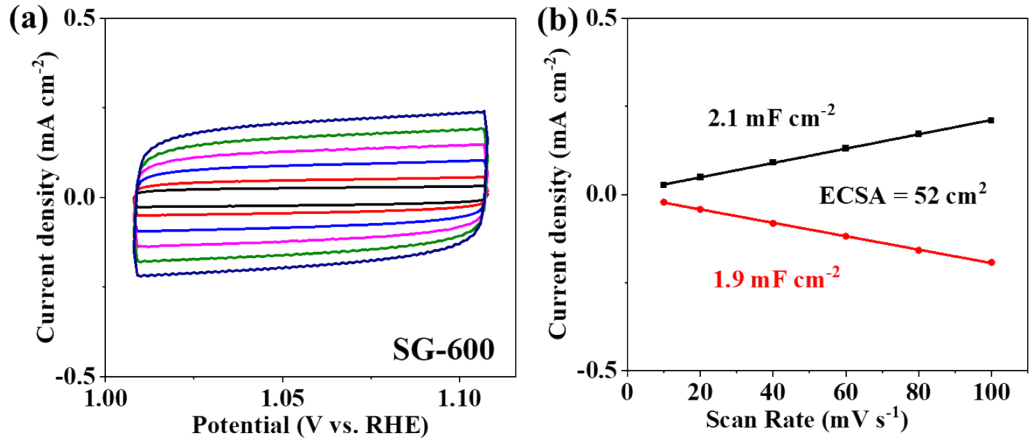

Fig. S5 Cyclic voltammogram curves of the SG-600 at different scan rates for the ORR.

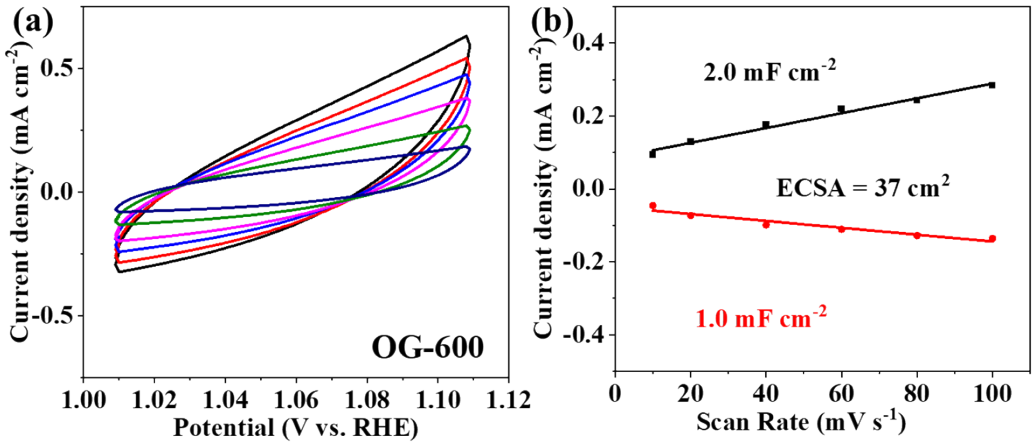

Fig. S6 Cyclic voltammogram curves of the OG-600 at different scan rates for the ORR.

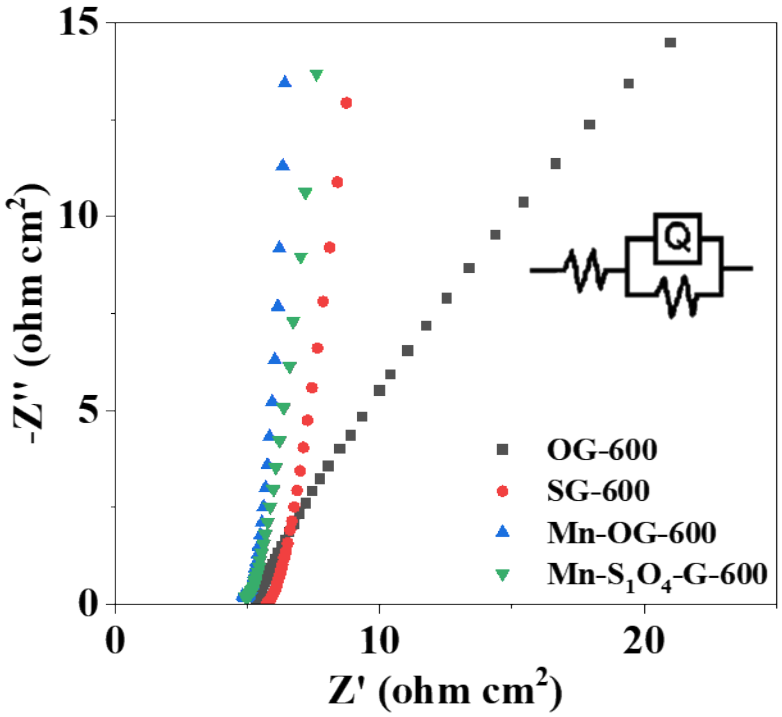

Fig. S7 Electrochemical impedance spectra (EIS) curves of different catalysts at 0.8 V vs. RHE.

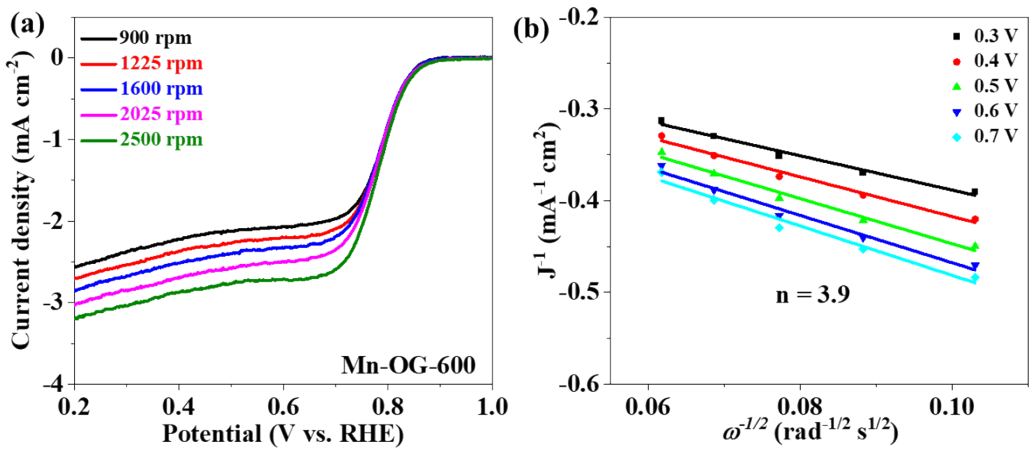

Fig. S8 (a) LSV curves of Mn-OG-600 at the different revolving speed from 900 rpm to 2500 rpm. (b) Koutecky-Levich plots and electron transfer number (*n*).

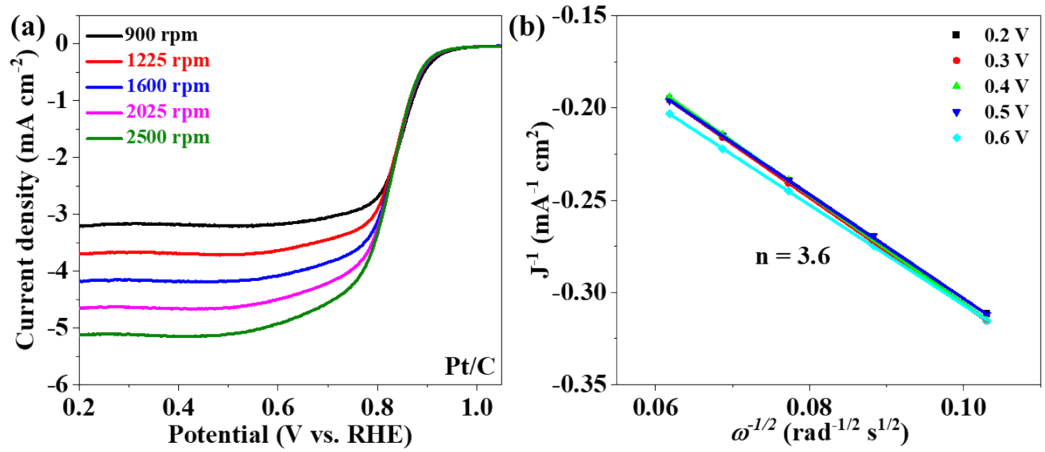

Fig. S9 (a) LSV curves of Pt/C at the different revolving speeds from 900 rpm to 2500 rpm. (b) Koutecky-Levich plots and electron transfer number (*n*).

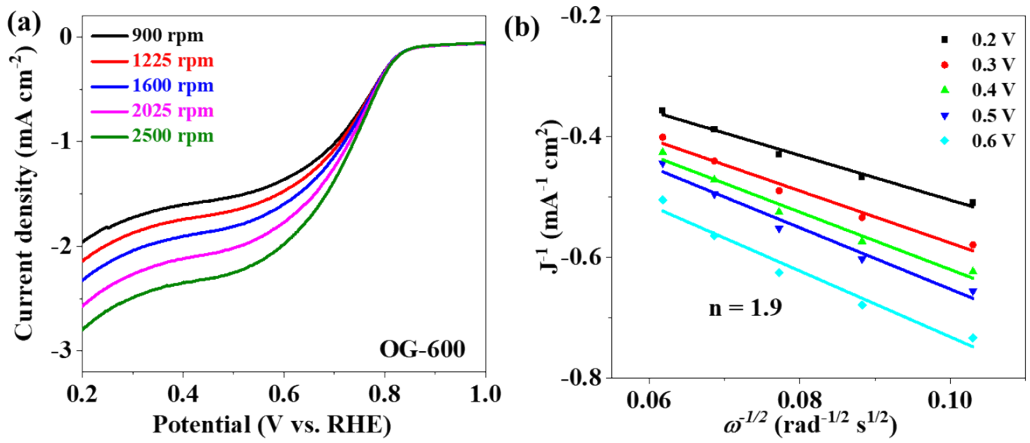

Fig. S10 (a) LSV curves of OG-600 at the different revolving speeds from 900 rpm to 2500 rpm. (b) Koutecky-Levich plots and electron transfer number (*n*).

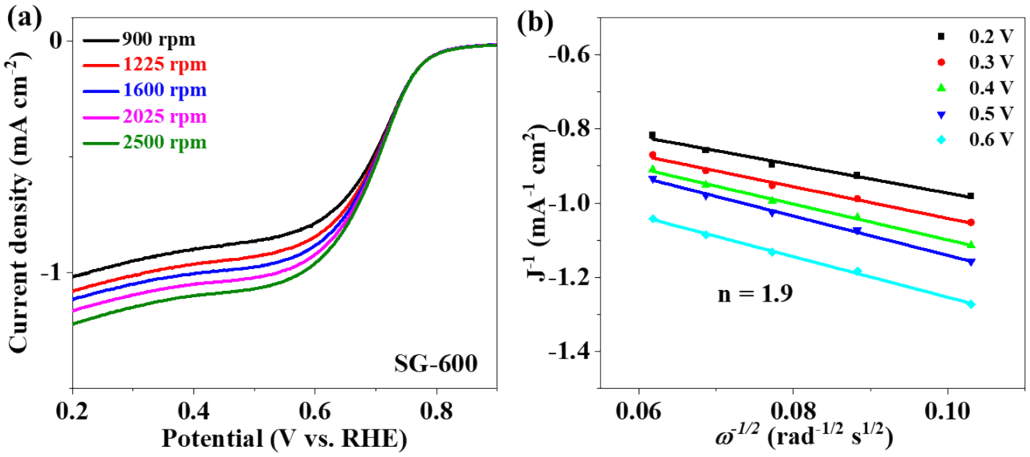

Fig. S11 (a) LSV curves of SG-600 at the different revolving speeds from 900 rpm to 2500 rpm. (b) Koutecky-Levich plots and electron transfer number (*n*).

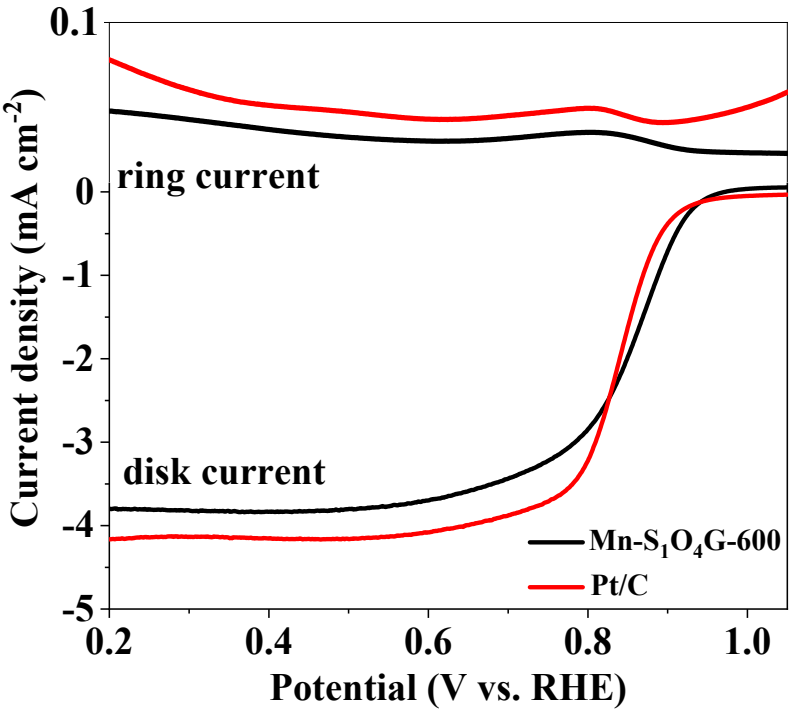

Fig. S12 The record ring and disk current of Pt/C and Mn-S_1O_4G-600.

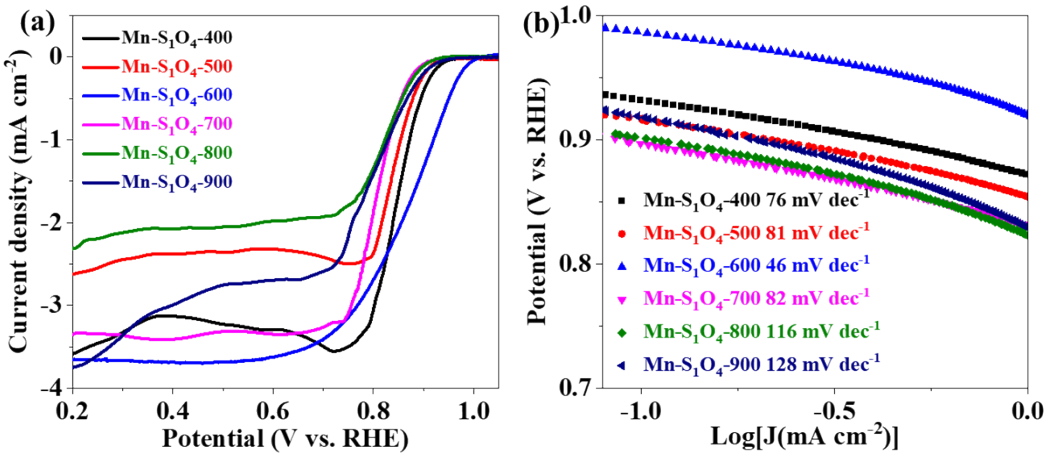

Fig. S13 (a) LSV curves and (b) Tafel plots for Mn-S_1O_4G-400, Mn-S_1O_4G-500, Mn-S_1O_4G-600, Mn-S_1O_4G-700, Mn-S_1O_4G-800, and Mn-S_1O_4G-900.

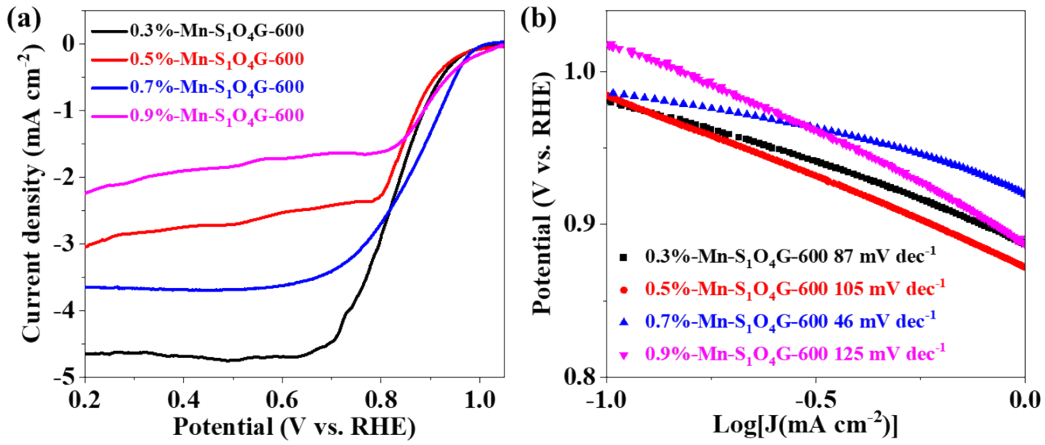

Fig. S14 (a) LSV curves and (b) Tafel plots for 0.3%-Mn-S_1O_4G-600, 0.5%-Mn-S_1O_4G-600, 0.7%-Mn-S_1O_4G-600, and 0.9%-Mn-S_1O_4G-600.

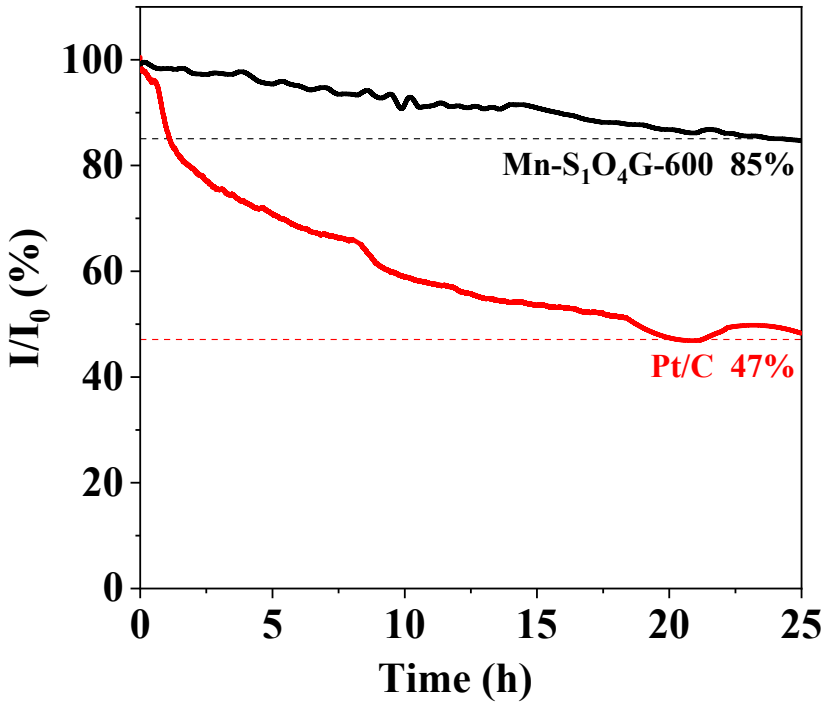

Fig. S15 Chronoamperometric (i-t) response of Mn-S_1O_4G-600 and Pt/C at 0.6 V.

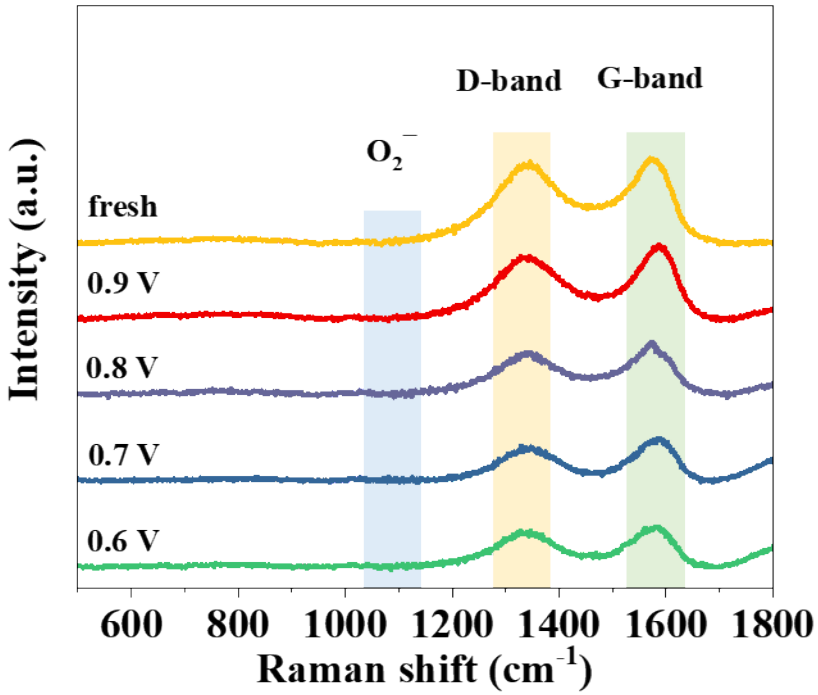

Fig. S16 In-situ Raman spectra of Mn-S_1O_4G-600 during the ORR process in 0.1 M KOH.

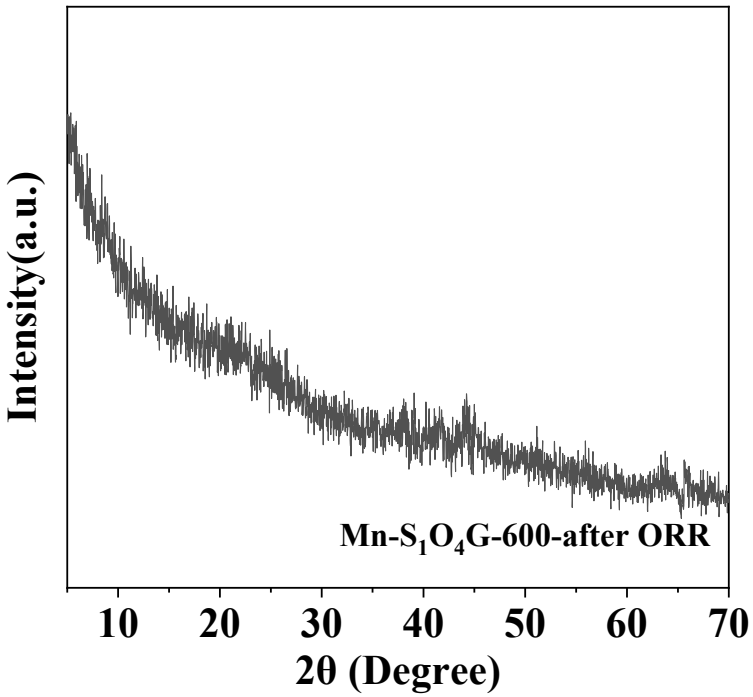

Fig. S17 XRD pattern of Mn-S_1O_4G-600 after ORR.

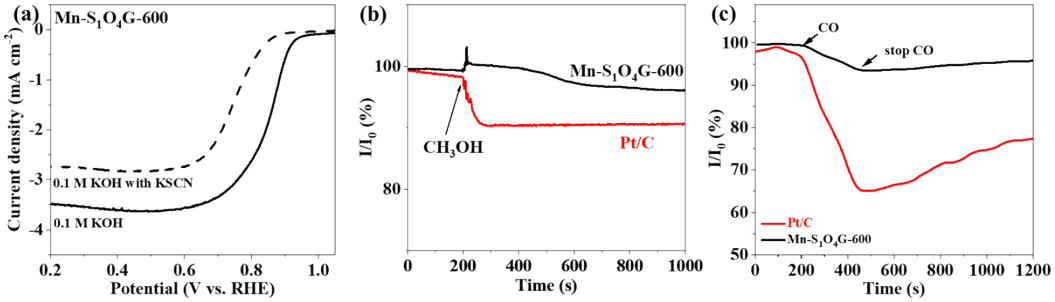

Fig. S18 (a) LSV curves of Mn-S_1O_4G-600 in 0.1 M KOH with 10 ppm KSCN. Poison experiment by (b) CH_3OH and (c) CO for Mn-S_1O_4G-600 and Pt/C.

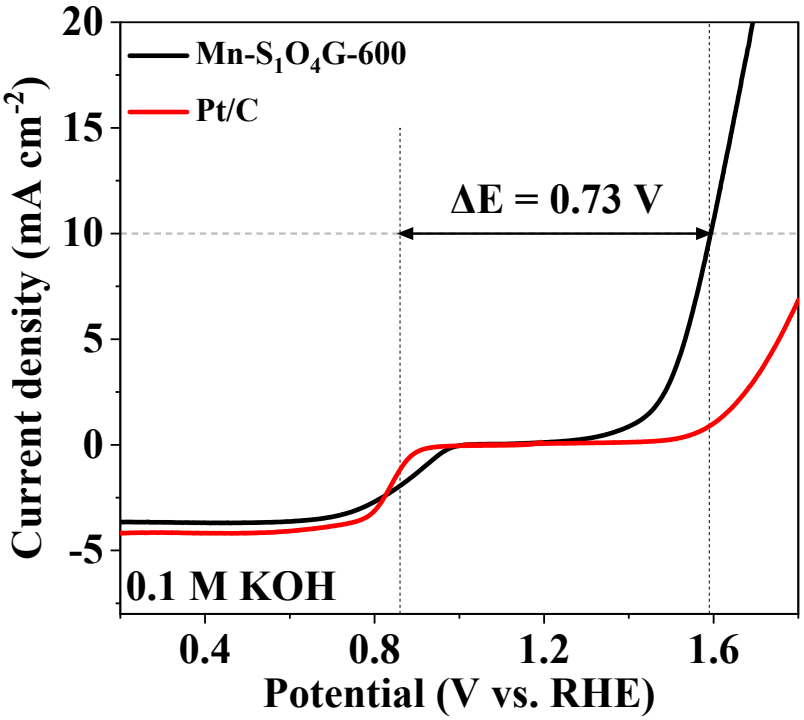

Fig. S19 The LSV curves of Mn-S_1O_4G-600 and Pt/C in 0.1 M KOH. The ΔE was the difference between η_{10} and $E_{1/2}$.

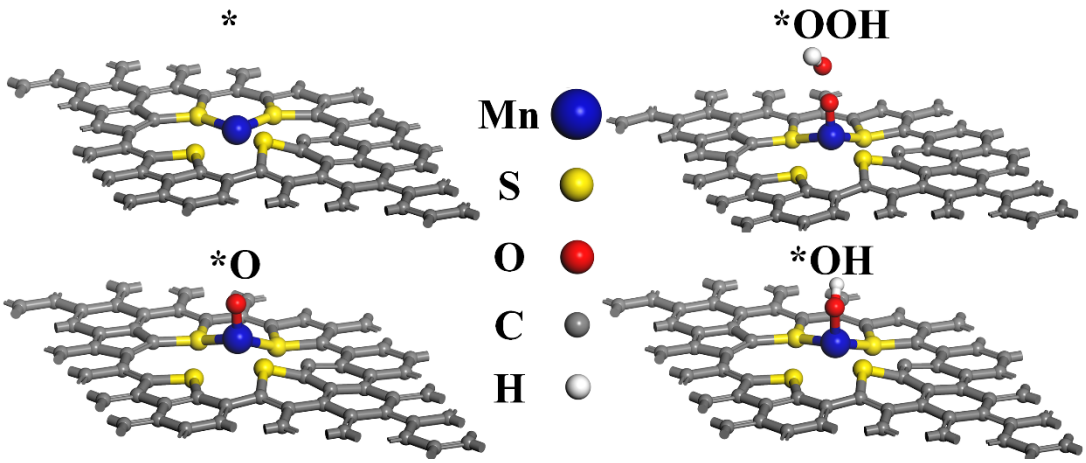

Fig. S20 The optimized structures of Mn-S_4G and the reaction intermediates.

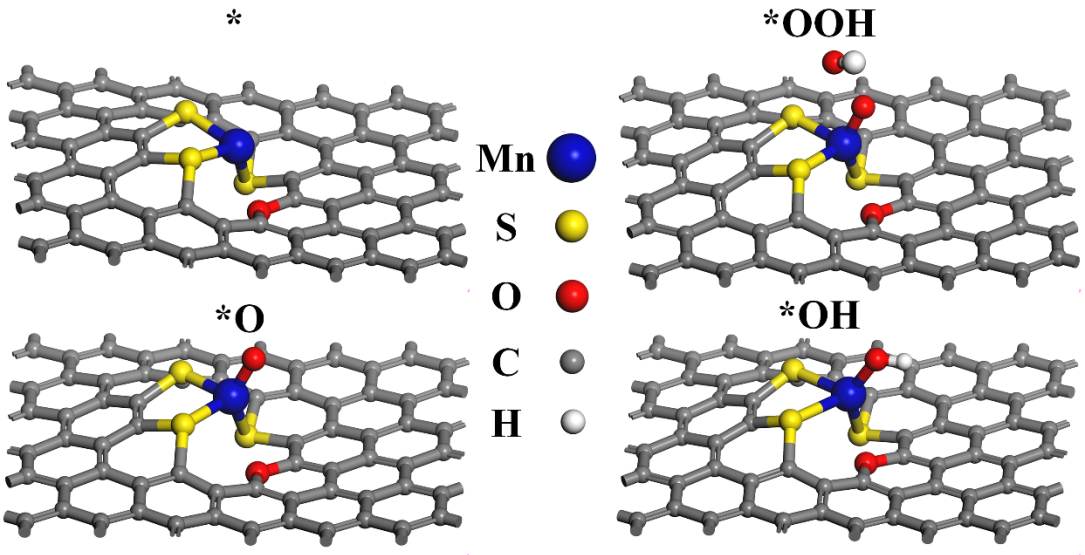

Fig. S21 The optimized structures of Mn-S_3OG and the reaction intermediates.

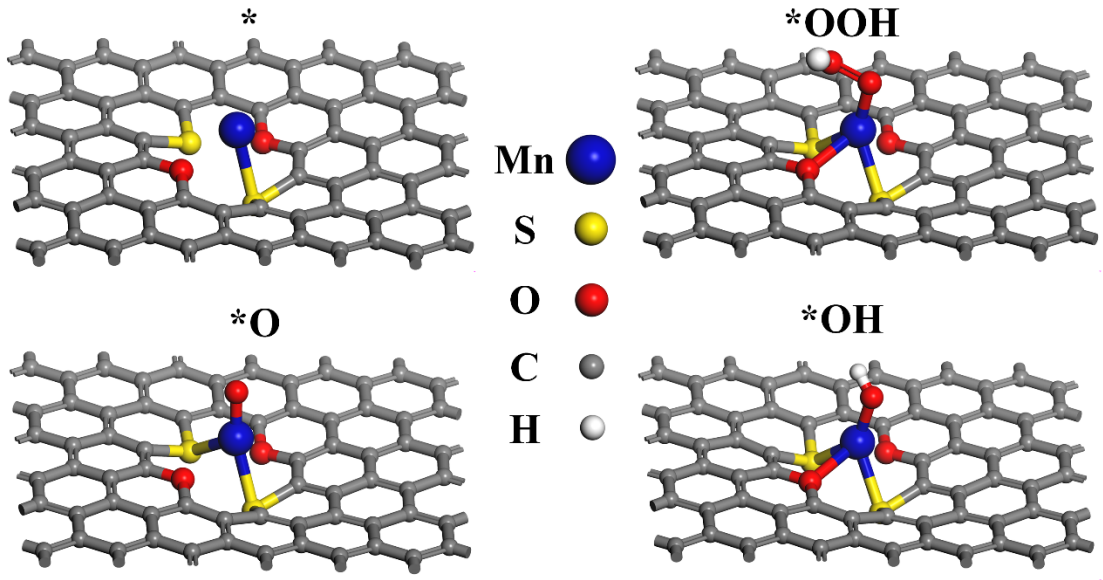

Fig. S22 The optimized structures of Mn-S_2O_2G and the reaction intermediates.

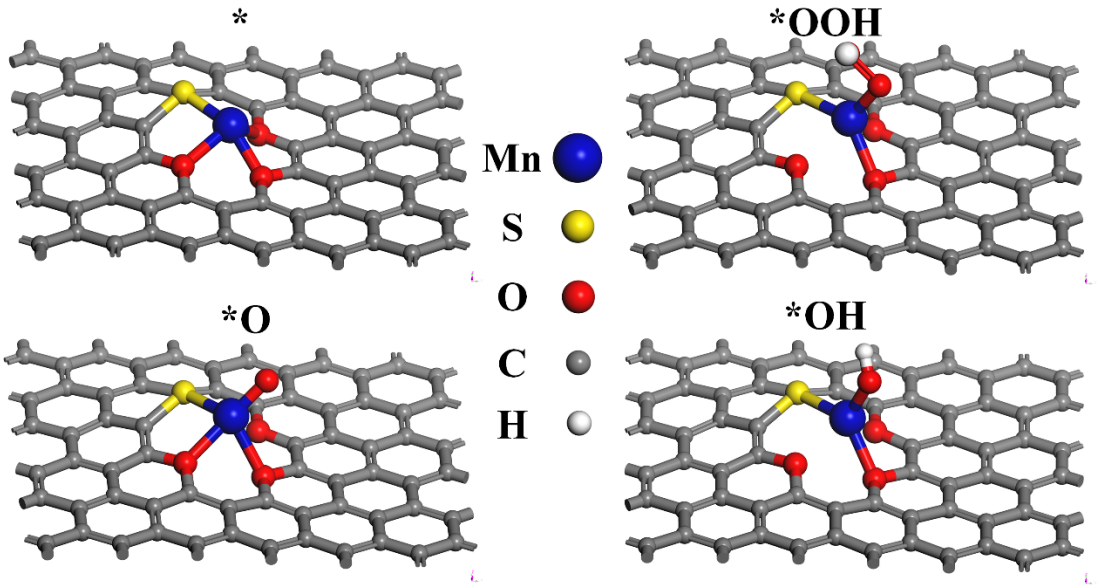

Fig. S23 The optimized structures of Mn-SO_3G and the reaction intermediates.

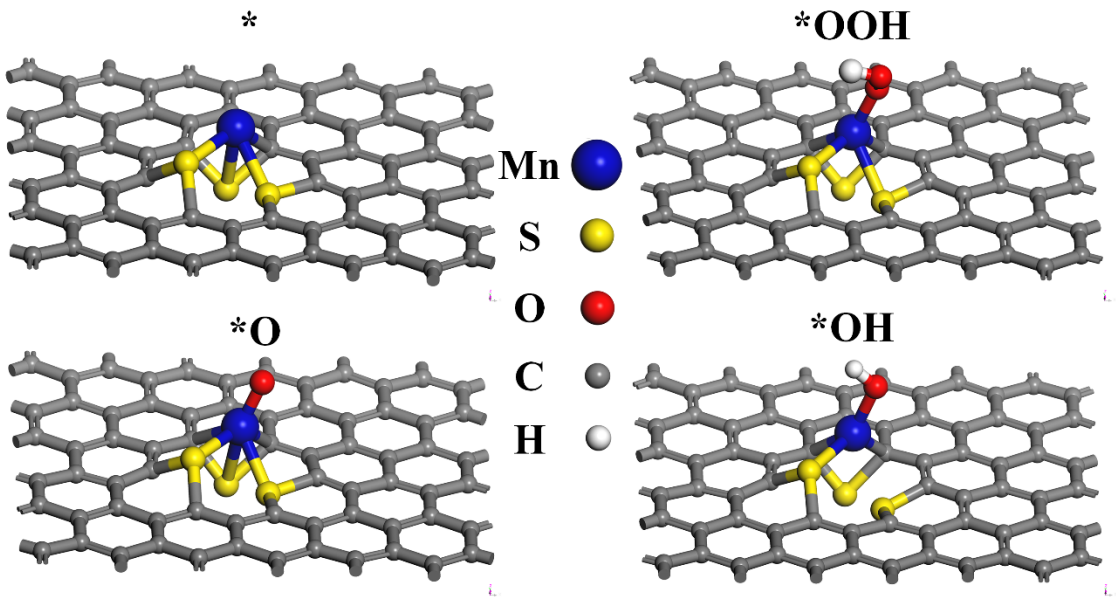

Fig. S24 The optimized structures of Mn-S_3G and the reaction intermediates.

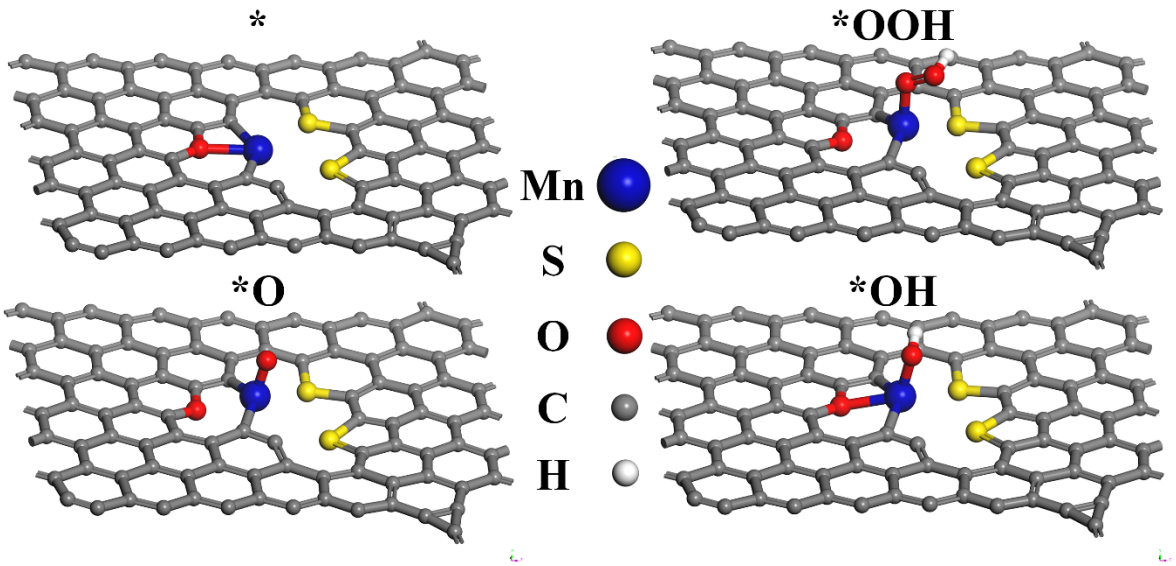

Fig. S25 The optimized structures of Mn-S_2OG and the reaction intermediates.

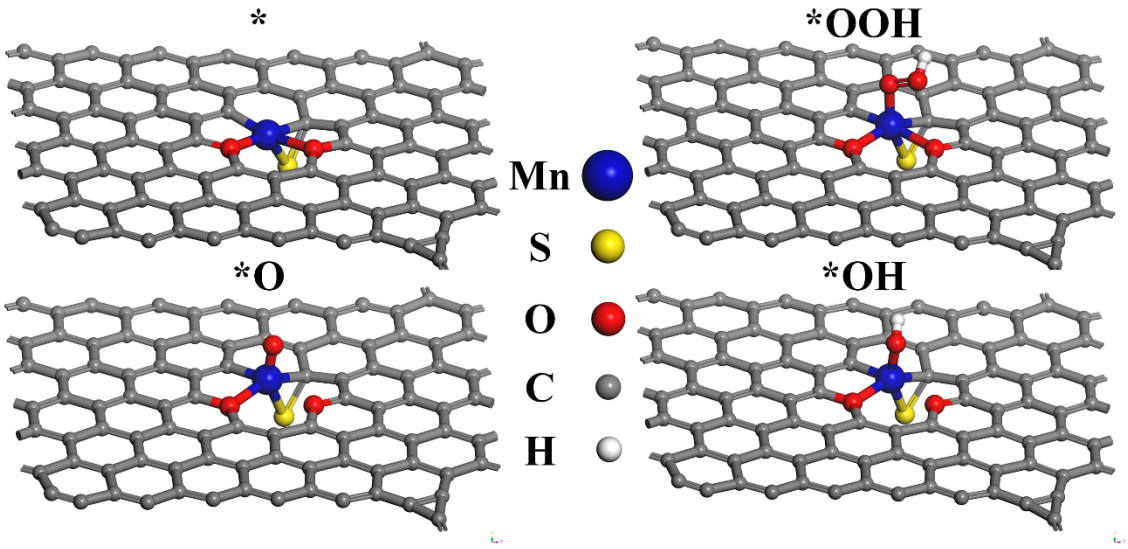

Fig. S26 The optimized structures of Mn-SO_2G and the reaction intermediates.

Table Sl. Curve fit parameters of Mn K-edge EXAFS for the Mn-S_1O_4G

Sample[a]	Path	N[b]	R/Å[c]	σ^2 (10^{-3}Å^2)[d]	ΔE_0/eV	R-factor
Mn-S_1O_4G	Mn-O	3.79±0.23	1.970±0.082	0.00455	1.987±1.58	0.018
	Mn-S	1.13±0.15	2.140±0.12	0.00236		

[a] S_0^2 was fixed as 0.9. [b] N is the coordination number. [c] R is the distance between absorber and backscatter atoms. [d] σ^2 is the Debye-Waller factor. R-factor is residual factor.

Table S2 ORR performance comparison of Mn-S_1O_4G-600 with other reported catalysts

catalysts	active site	E_{onset}	$E_{1/2}$	Tafel	Ref.
Mn-S_1O_4G-600	Mn-S_1O_4	0.98	0.86	46	This work
MSN200/CB	-	0.90	0.75	75	[3]
MnO_x@AC-S	NPs	0.914	0.82	-	[4]
MnO/N-rGO-800	NPs	0.90	0.81	-	[5]
MnO/N-rGO	NPs	0.85	0.77	-	[5]
Mn-NC-SA-950	Mn-N_5	-	0.852	49	[6]
Se@NC-1000	Se-C_2	0.95	0.85	52	[7]
Fe SA-NSC-900	Fe-N_3S	0.92	0.86	59	[8]
Cu-NSDC	Cu-S_1N_3	0.96	0.84	56	[9]

Cu-SA/NPSC	$Cu\text{-}S_1N_3$	0.90	0.84	57	[10]
Cu-N-CNFs	CuN_4	0.93	0.81	-	[11]
$Co\text{-}N_3C_1$-SAC	$Co\text{-}N_3C_1$	0.904	0.824	46	[12]
Cu/Zn-NC	ZnN_4 & CuN_4	0.98	0.83	54.8	[13]
FeNi SAs/NC	$Fe\text{-}Ni\text{-}N_6$	0.98	0.84	-	[14]

Table S3 ZAB performance comparison of Mn-S_1O_4G-600 with other reported catalysts.

Catalyst	Open-circuit voltage (V)	Maximum powder density (mW cm^{-2})	Specific capacity (mAh g^{-1})	Ref.
Mn-S_1O_4G-600	1.46	199	750	This work
Co_3Fe_7@Co/Fe-SAC	1.45	161	763	[15]
Fe-Co/N-HCS-x	1.019	244.6	804	[16]
Fe_3C|-N-C	1.414	63	-	[17]
PtFeNC	1.492	148	807	[18]
FeNi-NC	1.56	135.78	726.9	[19]
FeCo-NCNT	-	27.07	881.8	[20]
Co SA/NCFs	1.53	154.5	796	[21]
FePtNC	1.51	191.83	713	[22]
FeCo(a)-ACM	-	159.92	775.91	[23]
Ru–Cl–N SAC	1.455	205	804.26	[24]
Co@C-CoNC	-	162.80	810	[25]
ZnCo-PNC	1.49	142.6	793	[26]
IE-SAC(PA+MA)	1.42	62	690.3	[27]

References

1. W. S. Hummers, Jr. and R. E. Offeman, Preparation of Graphitic Oxide, *J. Am. Chem. Soc.*, 1958, **80**, 1339-1339.

2. S. E. Treimer, A. P.-C. Tang and D. C. J. E. Johnson, A Consideration of the Application of Koutecký-Levich Plots in the Diagnoses of Charge-Transfer Mechanisms at Rotated Disk Electrodes, 2002, **14**, 165-171.

3. J. X. Flores-Lasluisa, D. Salinas-Torres, M. V. López-Ramón, C. Moreno-Castilla, M. A. Álvarez, E. Morallón and D. Cazorla-Amorós, Electrocatalytic activity of calcined manganese ferrite solid nanospheres in the oxygen reduction reaction, *Environ. Res.*, 2022, **204**, 112126.

4. M. A. Marsudi, Y. Ma, B. Prakoso, J. J. Hutani, A. Wibowo, Y. Zong, Z. Liu and A. Sumboja, Manganese Oxide Nanorods Decorated Table Sugar Derived Carbon as Efficient Bifunctional Catalyst in Rechargeable Zn-Air Batteries.*Journal*, 2020, **10**.

5. I. J. R. Sarkar, S. G. Peera and R. Chetty, Manganese oxide nanoparticles supported nitrogen-doped graphene: a durable alkaline oxygen reduction electrocatalyst, *J. Appl. Electrochem.*, 2018, **48**, 849-865.

6. Y. Qin, C. Guo, Z. Ou, C. Xu, Q. Lan, R. Jin, Y. Liu, Y. Niu, Q. Xu, Y. Si and H. Li, Regulating single-atom Mn sites by precisely axial pyridinic-nitrogen coordination to stabilize the oxygen reduction, *J. Energy Chem.*, 2023, **80**, 542-552.

7. H. Hu, J. Wang, B. Cui, X. Zheng, J. Lin, Y. Deng and X. Han, Atomically Dispersed Selenium Sites on Nitrogen-Doped Carbon for Efficient

Electrocatalytic Oxygen Reduction, *Angew. Chem. Int. Ed.*, 2022, **61**, e202114441.

8. M. Wang, W. Yang, X. Li, Y. Xu, L. Zheng, C. Su and B. Liu, Atomically Dispersed Fe–Heteroatom (N, S) Bridge Sites Anchored on Carbon Nanosheets for Promoting Oxygen Reduction Reaction, *ACS Energy Lett.*, 2021, **6**, 379-386.

9. H. Zhang, Q. Sun, Q. He, Y. Zhang, X. He, T. Gan and H. Ji, Single Cu atom dispersed on S,N-codoped nanocarbon derived from shrimp shells for highly-efficient oxygen reduction reaction, *Nano Res.*, 2022, **15**, 5995-6000.

10. P. Chen, N. Zhang, T. Zhou, Y. Tong, W. Yan, W. Chu, C. Wu and Y. Xie, Tailoring Electronic Structure of Atomically Dispersed Metal–N3S1 Active Sites for Highly Efficient Oxygen Reduction Catalysis, *ACS Materials Letters*, 2019, **1**, 139-146.

11. F. Yan, L. Dong, J. Su, X. Liu, X. Han, J. Zang and Y. Wang, Copper coordinated with nitrogen in electrospun carbon nanofibers as a high-performance electrocatalyst for ORR, *Electrochem. Commun.*, 2022, **136**, 107245.

12. X. Hai, X. Zhao, N. Guo, C. Yao, C. Chen, W. Liu, Y. Du, H. Yan, J. Li, Z. Chen, X. Li, Z. Li, H. Xu, P. Lyu, J. Zhang, M. Lin, C. Su, S. J. Pennycook, C. Zhang, S. Xi and J. Lu, Engineering Local and Global Structures of Single Co Atoms for a Superior Oxygen Reduction Reaction, *ACS Catal.*, 2020, **10**, 5862-5870.

13. M. Tong, F. Sun, Y. Xie, Y. Wang, Y. Yang, C. Tian, L. Wang and H. Fu, Operando Cooperated Catalytic Mechanism of Atomically Dispersed Cu−N4 and Zn−N4 for Promoting Oxygen Reduction Reaction, *Angew. Chem. Int. Ed.*, 2021, **60**, 14005-14012.

14. D. Yu, Y. Ma, F. Hu, C.-C. Lin, L. Li, H.-Y. Chen, X. Han and S. Peng, Dual-Sites Coordination Engineering of Single Atom Catalysts for Flexible Metal–Air Batteries, *Adv. Energy Mater.*, 2021, **11**, 2101242.

15. B. Liu, S. Wang, R. Feng, Y. Ni, F. Song and Q. Liu, Anchoring Bimetal Single Atoms and Alloys on N-Doping-Carbon Nanofiber Networks for an Efficient Oxygen Reduction Reaction and Zinc–Air Batteries, *ACS Appl. Mater. Inter.*, 2022, **14**, 38739-38749.

16. Q. H. Nguyen, K. Im and J. Kim, Single atoms/metal nanoparticles-decorated hollow carbon spheres as oxygen reduction catalyst for zinc-air batteries, *Appl. Surf. Sci.*, 2024, **669**, 160497.

17. Y. Chen, X. Kong, Y. Wang, H. Ye, J. Gao, Y. Qiu, S. Wang, W. Zhao, Y. Wang, J. Zhou and Q. Yuan, A binary single atom Fe3C|FeNC catalyst by an atomic fence evaporation strategy for high performance ORR/OER and flexible Zinc-air battery, *Chem. Eng. J.*, 2023, **454**, 140512.

18. X. Zhong, S. Ye, J. Tang, Y. Zhu, D. Wu, M. Gu, H. Pan and B. Xu, Engineering Pt and Fe dual-metal single atoms anchored on nitrogen-doped carbon with high activity and durability towards oxygen reduction reaction for zinc-air battery, *Appl. Catal., B*, 2021, **286**, 119891.

19. C. Liu, S. Wu, S. Tian, J. Yang, J. Li, Q. Guan, F. Yin, X. Xiang, Y. Wang, X. Meng and Q. Yang, Structurally optimized rosette-like microspheres carbon with Fe-Ni single atom sites for bifunctional oxygen electrocatalysis in Zinc-Air batteries, *Chem. Eng. J.*, 2024, **497**, 154963.

20. Y. Tan, Y. Wang, A. Li, Y. Zhang, Y. Zhang and C. Cheng, Double synergetic FeCo-nanoparticles and single atoms embedded in N-doped carbon nanotube arrays as efficient bifunctional catalyst for high-performance zinc-air batteries, *Mater. Today Energy*, 2022, **29**, 101138.

21. Y. Han, H. Duan, C. Zhou, H. Meng, Q. Jiang, B. Wang, W. Yan and R. Zhang, Stabilizing Cobalt Single Atoms via Flexible Carbon Membranes as Bifunctional Electrocatalysts for Binder-Free Zinc–Air Batteries, *Nano Lett.*, 2022, **22**, 2497-2505.

22. W.-S. Song, M. Wang, X. Zhan, Y.-J. Wang, D.-X. Cao, X.-M. Song, Z.-A. Nan, L. Zhang and F. R. Fan, Modulating the electronic structure of atomically dispersed Fe–Pt dual-site catalysts for efficient oxygen reduction reactions, *Chem. Sci.*, 2023, **14**, 3277-3285.

23. C. Chen, D. Cheng, S. Liu, Z. Wang, M. Hu and K. Zhou, Engineering the multiscale structure of bifunctional oxygen electrocatalyst for highly efficient and ultrastable zinc-air battery, *Energy Storage Materials*, 2020, **24**, 402-411.

24. J. Chen, J. Huang, R. Wang, W. Feng, H. Wang, T. Luo, Y. Hu, C. Yuan, L. Feng, L. Cao, K. Kajiyoshi, C. He, Y. Liu, Z. Li and Y. Feng, Atomic ruthenium coordinated with chlorine and nitrogen as efficient and

multifunctional electrocatalyst for overall water splitting and rechargeable zinc-air battery, *Chem. Eng. J.*, 2022, **441**, 136078.

25. S. Chandrasekaran, R. Hu, L. Yao, L. Sui, Y. Liu, A. Abdelkader, Y. Li, X. Ren and L. Deng, Mutual Self-Regulation of d-Electrons of Single Atoms and Adjacent Nanoparticles for Bifunctional Oxygen Electrocatalysis and Rechargeable Zinc-Air Batteries, *Nano-Micro Lett.*, 2023, **15**, 48.

26. T. Najam, S. Shoaib Ahmad Shah, M. Sufyan Javed, P.-T. Chen, C. Chuang, A. Saad, Z. Song, W. Liu and X. Cai, Modulating the electronic structure of zinc single atom catalyst by P/N coordination and Co2P supports for efficient oxygen reduction in Zn-Air battery, *Chem. Eng. J.*, 2022, **440**, 135928.

27. K. Fan, Z. Li, Y. Song, W. Xie, M. Shao and M. Wei, Confinement Synthesis Based on Layered Double Hydroxides: A New Strategy to Construct Single-Atom-Containing Integrated Electrodes, *Adv. Funct. Mater.*, 2021, **31**, 2008064.